



Light propagation in biological tissue

Fatmir Asllanaj, Sylvain Contassot-Vivier, A. Hohmann, A. Kienle

► To cite this version:

Fatmir Asllanaj, Sylvain Contassot-Vivier, A. Hohmann, A. Kienle. Light propagation in biological tissue. *Journal of Quantitative Spectroscopy and Radiative Transfer*, 2019, 224, pp.78-90. 10.1016/j.jqsrt.2018.11.001 . hal-03514723

HAL Id: hal-03514723

<https://hal.science/hal-03514723>

Submitted on 6 Jan 2022

HAL is a multi-disciplinary open access archive for the deposit and dissemination of scientific research documents, whether they are published or not. The documents may come from teaching and research institutions in France or abroad, or from public or private research centers.

L'archive ouverte pluridisciplinaire **HAL**, est destinée au dépôt et à la diffusion de documents scientifiques de niveau recherche, publiés ou non, émanant des établissements d'enseignement et de recherche français ou étrangers, des laboratoires publics ou privés.

Light propagation in biological tissue

F. Asllanaj^{1,2,*}, S. Contassot-Vivier³, A. Hohmann⁴, A. Kienle⁴

¹ Université de Lorraine, LEMTA, UMR 7563, Vandœuvre-lès-Nancy, F-54500, France

² CNRS, LEMTA, UMR 7563, Vandœuvre-lès-Nancy, F-54500, France

³ Université de Lorraine, LORIA, UMR 7503 & AlGorille INRIA Project Team,
Vandœuvre-lès-Nancy, F-54500, France

⁴ Institut für Lasertechnologien in der Medizin und Meßtechnik an der Universität Ulm
Helmholtzstr.12, D-89081 Ulm, Germany

* Correspondence author - Phone : +33 3 72 74 42 73

E-mail: Fatmir.Asllanaj@univ-lorraine.fr

Abstract We developed a new parallel computational method for solving fluorescence and elastically scattered light propagation through a biological tissue illuminated by a collimated incident beam. The three-dimensional steady state radiative transfer equation was solved using a Modified Finite Volume Method with a cell-vertex formulation. An Exponential spatial differencing scheme was used to efficiently lessen the false scattering. Several test problems are presented to assess the performance and accuracy of the numerical Method. We show that it is possible to obtain a very good level of accuracy. Relative differences less than 1.5% were obtained in comparison with the Monte Carlo reference solution for the selected problems. This study shows the potential of the proposed computational method to be used as an accurate deterministic forward solver in Optical Tomography.

Keywords elastically scattered light, fluorescence light, biological tissue, radiative transfer equation, finite volume method, Monte Carlo method, parallel computing.

Nomenclature

A	surface area of cell, mm^2
C	concentration, $M = \text{mol mm}^{-3}$
D	distance, mm
G	isobarycentre

g	anisotropy factor of the Henyey-Greenstein phase function
i	integration point on surface panel
L	size of the medium, mm
l_a	absorption mean free path ($= 1/\mu_a$), mm
l_s	scattering mean free path ($= 1/\mu_s$), mm
l_t	transport mean free path ($= 1/\mu'_s$), mm
N	number of surface panels
n	refractive index
\mathbf{n}	outward unit vector normal to the medium boundary
p	scattering phase function, sr^{-1}
Q	source power density, W mm^{-3}
J^+	partial current or boundary photon flux, W mm^{-2}
R	radius, mm
\mathbf{r}	spatial position ($= x, y, z$), mm
S	source term in the medium, $\text{W mm}^{-3} \text{ sr}$
u	projection of integration point in an upstream position
V	control volume, mm^3

Greek symbols

σ	beam width, mm
$\Delta\Omega$	solid angle, sr
ΔP_j	plane orthogonal to the Ω direction that cross by the grid node P_j
ϵ	extinction coefficient, $\text{mm}^2 \text{ mol}^{-1} = \text{mm}^{-1} \text{ M}^{-1}$
η	fluorescence quantum yield
Γ	boundary of control volume
μ_a	absorption coefficient, mm^{-1}
$\mu_a^{x \rightarrow m}$	absorption coefficient of a fluorescent source in the tissue ($= C\epsilon$), mm^{-1}
Ω	direction vector
Ω	sub-domain
μ_t	attenuation coefficient ($= \mu_a + \mu_s$), mm^{-1}

ψ	radiance, $\text{W mm}^{-2} \text{ sr}^{-1}$
μ_s	scattering coefficient, mm^{-1}
μ_t	attenuation coefficient, $(= \mu_a + \mu_s)$, mm^{-1}
R	directional reflection coefficient
ρ	distance (radius), mm
Θ	angle between two directions
θ	polar angle
Υ	intensity of the collimated incident beam, $\text{W mm}^{-2} \text{ sr}$
\mathcal{T}	tetrahedron
\mathcal{J}	triangle
Φ	fluence rate, W mm^{-2}
ϕ	azimuthal angle

Subscripts

c	collimated
s	scattered
D	downstream
f	panel f
i_f	integration point on surface panel f
P	grid node
r	reference
t, v	(1, 2, 3), (4, 5, 6)
u_f	projection of i_f integration point in an upstream position
U	upstream
w	wall
x, y, z	(Ox)-axis, (Oy)-axis, (Oz)-axis

Superscripts

k	discrete angular direction
m	emission field
x	excitation field

1 Introduction

The use of the (VIS) Visible and NIR (Near-Infrared) light provides many possibilities, particularly for applications in biomedical diagnosis and treatment, such as optical tomography, laser surgery, and photodynamic therapy [1–3]. In the recent years, fluorescence molecular imaging has emerged as an investigative tool for pre-clinical imaging of optical reporter probes in small animals [2, 4]. This imaging technique uses fluorescent sources inside tissue as imaging contrast. In optical tomography, an inverse model aims at three-dimensional reconstruction of images based on light measurements collected at the tissue boundary [1–4]. The quality of the reconstructed image depends strongly on the accuracy of the forward solver. The Radiative Transfer Equation (RTE) is well acknowledged to accurately predict light propagation through biological tissues at both the meso and the macroscale [3, 4]. In the literature, very few papers present simulations of fluorescence light propagation through biological tissues using the RTE [5–12]. Generally, the numerical methods for solving the RTE can be classified into two groups: one is deterministic and based directly on the integro-partial differential equation; the other one is based on probabilistic formulations of the RTE such as Monte Carlo (MC) methods. MC methods are highly prevalent in many models of light propagation in biological tissue. Well-known drawbacks of these methods are their high computational costs and statistical errors. The use of MC models within image reconstruction in Optical Tomography for example is usually limited to the construction of a linear perturbation model for reconstructing the difference in optical properties from changes in the data [3]. Moreover, the inverse MC needs a huge number of photons to converge to the true optical properties. In contrast, the deterministic numerical methods can benefit from the efficient inversion techniques (based for example on the adjoint method) developed specifically for partial differential equations. Therefore, in this study, we are focusing on the deterministic numerical method. Different numerical methods were developed in the literature for solving the 3D RTE [13–23]. Due to the computationally expensive nature of the RTE and the challenging numerics, only few numerical solutions methods were developed for relevant 3D geometries using non-Cartesian grids [24–28] while those have important applications in biomedical optics. The numerical methods for solving the RTE cited above are quite interesting but present some shortcomings. For example, the angular discretizations of the RTE were performed using the DOM in [24–27, 30]. It is well known that one serious drawback of the DOM is the so-called "ray effect" which is a consequence of angular discretization [29–31]. In the particular case of anisotropic scattering, modelled with the Henyey-Greenstein (H-G) or Mie phase functions, the DOM does not strictly conserve energy, i.e., there is no guarantee that the integral of the scattering phase function over a unity spherical surface yields 4π , even though it is possible to use a correction factor of the in-scattering term to enforce conservation. However, the correction factor introduces changes in the overall shape and asymmetry factor of the phase function, and this may yield

large errors in the case of highly anisotropic phase functions. Hunter and Guo studied this problem the last years [32]. It was concluded that the FVM is more appropriate than the DOM for highly anisotropic scattering. In [30], a phase function normalization technique was employed to lessen the instability of the DOM. Note that Mohan et al. [28] reported that the P_N approximation does not suffer from the ray effect problem. Concerning the spatial differencing schemes, either the Step or Diamond schemes were used in [24–28]. The Step scheme, is only first-order accurate, and causes so-called false scattering (or numerical diffusion), whenever gradients of the radiance appear in directions not aligned with the direction of light propagation [29, 31]. False scattering can be sometimes lessen using grid refinement but this leads to a logical increase in computational time. The Diamond scheme, is formally second-order accurate, but it is not bounded, unlike the Step scheme. This means that physically unrealistic overshoots or undershoots, such as negative radiances, may appear in the numerical solution. Other more accurate spatial differencing schemes, such as the Positive and Exponential schemes were proposed in the literature. In particular, the Exponential scheme is generally regarded to be more accurate than the Step and Diamond schemes [29, 33].

The survey of the literature shows that no successful deterministic numerical solutions of the RTE (with realistic illumination and adapted to relevant 3D geometries) have been presented so far. In the present analysis, we tried to go beyond the previous studies by proposing a new computational method for solving light propagation based on the RTE. The remainder of this paper is organized as follows. Section two deals with the governing equations. The third section gives details of the numerical treatment of the RTE. The results obtained are presented and discussed in section four. Conclusions and future orientations are summarized in the final section.

2 Governing equations

2.1 Elastically scattered light

The RTE is an integro-differential equation, given by [3, 4]:

$$\left(\boldsymbol{\Omega} \cdot \boldsymbol{\nabla} + \mu_t(\mathbf{r})\right)\psi(\mathbf{r}, \boldsymbol{\Omega}) = \mu_s(\mathbf{r}) \int_{\Omega'=4\pi} p(\boldsymbol{\Omega}' \cdot \boldsymbol{\Omega}) \psi(\mathbf{r}, \boldsymbol{\Omega}') d\Omega' + S(\mathbf{r}, \boldsymbol{\Omega}), \quad (1)$$

where $\psi(\mathbf{r}, \boldsymbol{\Omega})$ is the radiance at location \mathbf{r} in direction $\boldsymbol{\Omega}$, μ_t and μ_s are the attenuation and scattering coefficients of medium, respectively. The function $p(\boldsymbol{\Omega}' \cdot \boldsymbol{\Omega})$ is the scattering phase function which is normalized to unity. The function $S(\mathbf{r}, \boldsymbol{\Omega})$ represents any source term in the medium.

Partial reflection of light at the medium-air interface is caused by the refractive index mismatch of both media. The fraction of reflected light is given by the directional reflection coefficient R . For a semi-transparent interface, illuminated

by an external light source Υ , the partly-reflecting boundary specifies the radiance as the sum of two contributions [4, 29]:

$$\psi(\mathbf{r}, \mathbf{\Omega}) = \Upsilon(\mathbf{r}, \mathbf{\Omega}) + R(\Theta) \psi(\mathbf{r}, \mathbf{\Omega}_{sp}) \quad \text{for } \mathbf{\Omega} \cdot \mathbf{n} < 0 \quad \text{and} \quad \cos \Theta = \mathbf{\Omega}_{sp} \cdot \mathbf{n} = -\mathbf{\Omega} \cdot \mathbf{n}, \quad (2)$$

where \mathbf{n} is the local outward unit vector normal to the medium boundary and $\mathbf{\Omega}_{sp}$ is the direction of specular reflection.

2.2 Fluorescence light

The generation and propagation of fluorescent light in the medium can be accurately modeled by a set of two coupled RTEs in the steady-state domain [4, 7] as described below.

2.2.1 Excitation light propagation

The equation that describes the excitation light propagation emanating from the external light source at wavelength λ^x is:

$$\left(\mathbf{\Omega} \cdot \nabla + \mu_t^x(\mathbf{r}) + \mu_a^{x \rightarrow m}(\mathbf{r}) \right) \psi^x(\mathbf{r}, \mathbf{\Omega}) = \mu_s^x(\mathbf{r}) \int_{\Omega'=4\pi} p^x(\mathbf{\Omega}' \cdot \mathbf{\Omega}) \psi^x(\mathbf{r}, \mathbf{\Omega}') d\Omega', \quad (3)$$

where $\psi^x(\mathbf{r}, \mathbf{\Omega})$ is the excitation radiance at location \mathbf{r} in direction $\mathbf{\Omega}$, while $\mu_a^{x \rightarrow m}$ is the absorption coefficient of a fluorescent source in tissue at the excitation wavelength λ^x .

The boundary conditions for the excitation light at λ^x are given with:

$$\psi^x(\mathbf{r}, \mathbf{\Omega}) = \Upsilon^x(\mathbf{r}, \mathbf{\Omega}) + R(\Theta) \psi^x(\mathbf{r}, \mathbf{\Omega}_{sp}) \quad \text{for } \mathbf{\Omega} \cdot \mathbf{n} < 0, \quad (4)$$

where $\Upsilon^x(\mathbf{r}, \mathbf{\Omega})$ is an external source which illuminates the tissue surface at wavelength λ^x .

The excitation light fluence at location \mathbf{r} is defined as:

$$\Phi^x(\mathbf{r}) = \int_{\Omega=4\pi} \psi^x(\mathbf{r}, \mathbf{\Omega}) d\Omega. \quad (5)$$

2.2.2 Emission light propagation

The light propagation at the emission wavelength λ^m due to the fluorescent source in tissue is modelled as:

$$\left(\mathbf{\Omega} \cdot \nabla + \mu_t^m(\mathbf{r}) \right) \psi^m(\mathbf{r}, \mathbf{\Omega}) = \mu_s^m(\mathbf{r}) \int_{\Omega'=4\pi} p^m(\mathbf{\Omega}' \cdot \mathbf{\Omega}) \psi^m(\mathbf{r}, \mathbf{\Omega}') d\Omega' + Q^m(\mathbf{r}), \quad (6)$$

where $\psi^m(\mathbf{r}, \mathbf{\Omega})$ denotes the emission radiance at location \mathbf{r} in direction $\mathbf{\Omega}$. The fluorescence source term which represents the fluorescence emission by the fluorescent source is given by:

$$Q^m(\mathbf{r}) = \frac{1}{4\pi} \eta \mu_a^{x \rightarrow m}(\mathbf{r}) \Phi^x(\mathbf{r}). \quad (7)$$

where η is the fluorescence quantum yield. The boundary conditions for the emitted light at λ^m are given with:

$$\psi^m(\mathbf{r}, \mathbf{\Omega}) = R(\Theta) \psi^m(\mathbf{r}, \mathbf{\Omega}_{sp}) \quad \text{for } \mathbf{\Omega} \cdot \mathbf{n} < 0. \quad (8)$$

3 Numerical treatment

3.1 Problem statement

A 3D absorbing and highly-forward scattering medium such as a biological tissue illuminated by a collimated incident beam (denoted Υ) is studied. Part of the beam propagates through the medium without being deviated, while the rest is scattered in all directions. It is thus convenient to split the radiance ψ into two components. These are denoted $\psi_c(\mathbf{r}) = \psi(\mathbf{r}, \mathbf{\Omega})\delta(\mathbf{\Omega} - \mathbf{\Omega}_c)$ (δ is the Dirac-delta function and $\mathbf{\Omega}_c$ is the direction of the collimated incident beam) and $\psi_s(\mathbf{r}, \mathbf{\Omega})$. They are respectively the collimated and scattered components of radiance [34]. The $\psi_c(\mathbf{r})$ collimated radiance is governed by the Bouguer-Beer-Lambert attenuation law:

$$\psi_c(\mathbf{r}) = \Upsilon(\mathbf{r}_w) \exp \left[- \int_{\mathbf{r}_w}^{\mathbf{r}} \mu_t(\mathbf{u}) du \right], \quad (9)$$

where the integration is performed on the optical path in $\mathbf{\Omega}_c$ direction from the point \mathbf{r}_w at the illuminated boundary, to the point \mathbf{r} in the medium. The scattered radiance $\psi_s(\mathbf{r}, \mathbf{\Omega})$ is the solution of the RTE (1) (or (3) in case of the fluorescence light) with a radiation source term due to the scattered part of the incident beam [34]:

$$S_c(\mathbf{r}, \mathbf{\Omega}) = \mu_s(\mathbf{r}) p(\mathbf{\Omega}_c \cdot \mathbf{\Omega}) \psi_c(\mathbf{r}), \quad (10)$$

and with the following boundary conditions:

$$\psi_s(\mathbf{r}, \mathbf{\Omega}) = R(\Theta) \psi_s(\mathbf{r}, \mathbf{\Omega}_{sp}) \quad \text{for} \quad \mathbf{\Omega} \cdot \mathbf{n} < 0. \quad (11)$$

The H-G phase function is the most widely-adopted scattering phase function of biomedical optics and this has been used here [4]. As for the radiance, it is convenient to split the fluence distribution into two components, denoted Φ_c and Φ_s , which are respectively the collimated and scattered components of fluence. Then, $\Phi(\mathbf{r}) = \Phi_c(\mathbf{r}) + \Phi_s(\mathbf{r})$ with,

$$\Phi_c(\mathbf{r}) = \psi_c(\mathbf{r}) \quad \text{and} \quad \Phi_s(\mathbf{r}) = \int_{4\pi} \psi_s(\mathbf{r}, \mathbf{\Omega}) d\Omega. \quad (12)$$

The detector readings at the medium surface are obtained from the exiting partial current or photon boundary flux. At each boundary point, we have:

$$J^+(\mathbf{r}) = \int_{\mathbf{\Omega} \cdot \mathbf{n} > 0} [1 - R(\Theta)] \psi_s(\mathbf{r}, \mathbf{\Omega}) \mathbf{\Omega} \cdot \mathbf{n} d\Omega \quad \left(+ [1 - R(\Theta_c)] \psi_c(\mathbf{r}) (\mathbf{\Omega}_c \cdot \mathbf{n}) \text{ if } \mathbf{\Omega}_c \cdot \mathbf{n}(\mathbf{r}) > 0 \right), \quad (13)$$

with $\cos \Theta = \mathbf{\Omega} \cdot \mathbf{n}$ and $\cos \Theta_c = \mathbf{\Omega}_c \cdot \mathbf{n}$. It should be noted that the reflectance (resp. transmittance) corresponds to the outgoing flux at the medium surface (resp. opposite medium surface) that is illuminated.

3.2 Angular and spatial discretizations of the computational domain

The angular discretization of the RTE requires the selection of a finite number of directions of light propagation and the selection of discrete solid angles, also referred to as control angles. The simplest angular discretization method consists of the division of the angular domain into a finite number of discrete, nonoverlapping, solid angles $m \in \{1, \dots, N_{dir}\}$ (N_{dir} is the total number of discrete solid angles) defined by the intersection of lines of constant latitude and lines of constant longitude. This choice is typical of the FVM and was used here. The recent applications of 3D optical imaging through biological tissues by use of light requires modeling of geometrically complex boundaries at the tissue-air interface or at the tumor-like inclusion. To this end, the computational spatial domain which interested us was divided into four-node tetrahedral elements using unstructured grids (like those used in MRI imaging for example). Here, a cell-vertex formulation was adopted for the control volumes. It consists in building control volumes around each node of the grid. Those are polyhedrons with quadrilateral faces. The V_P control volume surrounding node \mathbf{P} was built with all tetrahedrons having node \mathbf{P} as vertex. Γ_P is the boundary of V_P and represents a surface here. For each of these tetrahedrons (which have in common node \mathbf{P}), a partial volume (which is a part of V_P) is described in Fig. 1(a). To explain the construction of a control volume (a polyhedron in this case), the construction of a partial volume from a tetrahedron is detailed. Let us consider, for example, a $\mathcal{T} = (\mathbf{P}_1, \mathbf{P}_2, \mathbf{P}_3, \mathbf{P}_4)$ tetrahedron with the V_{P_1} partial volume surrounding node \mathbf{P}_1 (Fig. 1(a)). Then, V_{P_1} is a hexahedron with six quadrilateral faces, 12 edges and 8 vertices. It is defined by the \mathbf{P}_1 nodal node and,

- the isobarycentre of \mathcal{T} denoted by \mathbf{G}_T ;
- the three medium points denoted by $\mathbf{P}_{12}, \mathbf{P}_{13}, \mathbf{P}_{14}$ respectively of edges $[\mathbf{P}_1\mathbf{P}_2], [\mathbf{P}_1\mathbf{P}_3], [\mathbf{P}_1\mathbf{P}_4]$;
- the three isobarycentres denoted by $\mathbf{G}_1, \mathbf{G}_2, \mathbf{G}_3$ respectively of triangles $(\mathbf{P}_1, \mathbf{P}_2, \mathbf{P}_3), (\mathbf{P}_1, \mathbf{P}_2, \mathbf{P}_4), (\mathbf{P}_1, \mathbf{P}_3, \mathbf{P}_4)$.

Thus, each control volume is described by the volume of several hexahedrons. It should be noted at this point that a V_P control volume has as many hexahedrons as tetrahedrons having node \mathbf{P} as vertex. For each hexahedron (partial volume) belonging to V_P , there are three faces belonging to Γ_P . On the hexahedron shown in Fig. 1(a), these three faces correspond to the three quadrilaterals $(\mathbf{G}_T, \mathbf{G}_1, \mathbf{p}_{12}, \mathbf{G}_2)$, $(\mathbf{G}_T, \mathbf{G}_1, \mathbf{p}_{13}, \mathbf{G}_3)$ and $(\mathbf{G}_T, \mathbf{G}_2, \mathbf{p}_{14}, \mathbf{G}_3)$. Each of these quadrilaterals, defined as panel f , is a partial surface of Γ_P . The Γ_P surface is subdivided into N_f surface panels and in the centre of these the \mathbf{i}_f integration points are defined as illustrated in Fig. 1(b). The number of surface panels varies from one control volume to another. For a panel f , \mathbf{i}_f is the integration point located at the centre of gravity of the panel, A_f is its surface area, and \mathbf{n}_f is the outward unit vector normal to the panel f (Fig. 1(b)). The advantage of this construction is that it perfectly defines the integration points since they rise directly from the grid nodes.

[Figure 1 about here.]

3.3 Phase function normalization

In the modified FVM presented below, the RTE must be integrated into a $\Delta\Omega^k$ control solid angle centered around a Ω^k discrete angular direction [34]. The normalization procedure is expressed as follows:

$$\tilde{p}^{k',k} = \frac{1}{\Delta\Omega^{k'} \Delta\Omega^k} \int_{\Delta\Omega^k} \int_{\Delta\Omega^{k'}} p(\Omega' \cdot \Omega) d\Omega' d\Omega \quad ; \quad \tilde{p}^{k_c,k} = \frac{1}{\Delta\Omega^k} \int_{\Delta\Omega^k} p(\Omega_c \cdot \Omega) d\Omega, \quad (14)$$

where $\Delta\Omega^{k'}$, $\Delta\Omega^k$ are control solid angles centered around the $\Omega^{k'}$, Ω^k discrete angular directions respectively. $\tilde{p}^{k',k}$ is the average scattering phase function between control solid angles $\Delta\Omega^{k'}$ and $\Delta\Omega^k$. The collimated direction is indicated by k_c . A quadrature rule was used to compute the integrals in (14) by splitting the control solid angles into smaller angles.

3.4 FVM applied to the RTE

The RTE (1) with a general source term S can be taken as reference for the application of the FVM presented below. In the case of elastically scattered light and excitation light, $S = S_c$ given by (10). In the case of emission light, from Eq. (6), $S = Q^m$ with Q^m given by (7). In order to apply the FVM to the RTE, the quantities (ψ , ψ_c , S , Φ^x) and the optical properties (μ_a , μ_s , $\mu_a^{x \rightarrow m}$) are assumed to be constant over a sufficiently small V_P control volume (taking only one value at node P) and within a $\Delta\Omega^k$ control solid angle centered around an Ω^k discrete angular direction. The integration of the RTE, over each control volume and each solid angle in which the space is discretized yields (applying the Gauss divergence theorem) the following algebraic equation [29, 34]:

$$\sum_{f=1}^{N_f} \psi_{i_f}^k A_f \Delta_f^k = \left\{ -\mu_{t,P} \psi_P^k + \mu_{s,P} \sum_{k'=1}^N \tilde{p}^{k',k} \psi_P^{k'} \Delta\Omega^{k'} + S_P^k \right\} \Delta\Omega^k V_P, \quad (15)$$

where $\psi_{i_f}^k$ is an approximation of the radiance at the i_f integration point and in the Ω^k discrete direction. The quantity:

$$\Delta_f^k = \int_{\Delta\Omega^k} \Omega \cdot \mathbf{n}_f d\Omega, \quad (16)$$

is an integral which depends only on the orientation of the surface element f for the direction considered. It should be noted that the second quantity:

$$\Delta\Omega^k = \int_{\Delta\Omega^k} d\Omega, \quad (17)$$

and also (16) are, in our case, evaluated analytically (which is not the case for the DOM) using the angular discretisation with a constant step. This leads to a better accuracy. In the case of the elastically scattered light and the excitation light,

the following relation yields from Eqs. (10) and (14):

$$S_P^k = S_{c,P}^k = \mu_{s,P} \tilde{p}^{k_c,k} \psi_P^{k_c}, \quad (18)$$

In the case of emission light, it follows from Eqs. (6) and (7):

$$S_P^k = Q_P^m = \frac{1}{4\pi} \eta \mu_{a,P}^{x \rightarrow m} \Phi_P^x. \quad (19)$$

3.5 Spatial discretization of the transport term of the radiance

False scattering may be successfully lessen using appropriate closure relations. To solve the set of equations (15), closure relations between the $\psi_{i_f}^k$ integration-point values and the nodal values of the radiance are needed (Fig. 1(a)). The directional nature of light propagation needed to be taken into account in order to establish the closure relations. Thus, for a specific direction of light propagation, only the nodal values located upstream from the integration-point should be considered. It is known that the Step scheme causes strong false scattering while the Diamond scheme may yield oscillatory solutions. The Exponential scheme relies on the integral form of the RTE and is expected to be more accurate than the other two schemes [29,33]. Finally, we opted to use the Exponential scheme in the present study.

3.5.1 The Exponential scheme

As presented in [34], a locally rigorous one-dimensional integration of the RTE along the optical path $(\mathbf{u}_f, \mathbf{i}_f)$ of Ω direction with \mathbf{u}_f located upstream from \mathbf{i}_f was used:

$$\begin{aligned} \psi(\mathbf{i}_f, \Omega) &= \psi(\mathbf{u}_f, \Omega) \exp \left[- \int_{\mathbf{u}_f}^{\mathbf{i}_f} \mu_t(\mathbf{s}) ds \right] \\ &+ \int_{\mathbf{u}_f}^{\mathbf{i}_f} \left\{ S(\mathbf{s}, \Omega) + \mu_s(\mathbf{s}) \int_{\Omega'=2\pi} p(\Omega' \cdot \Omega) \psi(\mathbf{s}, \Omega') d\Omega' \right\} \exp \left[- \int_{\mathbf{s}}^{\mathbf{i}_f} \mu_t(\mathbf{u}) du \right] ds. \end{aligned} \quad (20)$$

The following approximation can be used, $\psi(\mathbf{s}, \Omega') \approx \psi(\mathbf{u}_f, \Omega')$ for $\mathbf{s} \in (\mathbf{u}_f, \mathbf{i}_f)$. To compact the equations, the following notations are introduced:

$$\begin{aligned} D_f^k &= A_f \Delta_f^k \exp \left[- \int_{\mathbf{u}_f}^{\mathbf{i}_f} \mu_t(\mathbf{s}) ds \right] ; \quad E_f^k = A_f \Delta_f^k \int_{\mathbf{u}_f}^{\mathbf{i}_f} \mu_s(\mathbf{s}) \exp \left[- \int_{\mathbf{s}}^{\mathbf{i}_f} \mu_t(\mathbf{u}) du \right] ds, \\ C_f^k &= A_f \Delta_f^k \int_{\mathbf{u}_f}^{\mathbf{i}_f} S^k(\mathbf{s}) \exp \left[- \int_{\mathbf{s}}^{\mathbf{i}_f} \mu_t(\mathbf{u}) du \right] ds. \end{aligned} \quad (21)$$

with $\Delta_f^k = |\mathbf{u}_f - \mathbf{i}_f|$ the optical path length in Ω^k direction from the point \mathbf{u}_f to the point \mathbf{i}_f .

If $S = S_c$, from Eqs. (10) and (14), an approximate value of C_f^k can be deduced:

$$C_f^k \approx \frac{1}{2} \left(\psi_c(\mathbf{i}_f) + \psi_c(\mathbf{u}_f) \right) \tilde{p}^{k_c,k} E_f^k, \quad (22)$$

In the case of emission light, $S = Q^m$ and from Eqs. (6) and (7), it follows:

$$C_f^k \approx A_f \Delta_f^k \frac{\eta}{4\pi} \frac{1}{2} \left(\mu_{a,i_f}^{x \rightarrow m} \Phi_{x,i_f} + \mu_{a,u_f}^{x \rightarrow m} \Phi_{x,u_f} \right) \int_{\mathbf{u}_f}^{\mathbf{i}_f} \exp \left[- \int_{\mathbf{s}}^{\mathbf{i}_f} \mu_t(\mathbf{u}) du \right] ds. \quad (23)$$

Combining Eqs. (20) and (21) in Eq. (15), we obtain:

$$\sum_{f=1}^{N_f} \psi_{i_f}^k A_f \Delta_f^k = \sum_{f=1}^{N_f} \psi_{u_f}^k D_f^k + \sum_{f=1}^{N_f} \left\{ \sum_{k'=1}^N \tilde{p}^{k',k} \psi_{u_f}^{k'} \Delta \Omega^{k'} \right\} E_f^k + \sum_{f=1}^{N_f} C_f^k. \quad (24)$$

The projections and linear interpolations presented below were expected to improve the closure relations and the accuracy of the results. Also, they were used to link $\psi_{u_f}^k$ defined at the \mathbf{u}_f point with the nodal values of the radiance.

3.5.2 Projections and linear interpolations

To simplify the equations presented further, a notation was introduced: $(\mathbf{A}, \mathbf{B}, \dots) \leq (\mathbf{C}, \mathbf{D}, \dots)$ means points $(\mathbf{A}, \mathbf{B}, \dots)$ are located upstream from points $(\mathbf{C}, \mathbf{D}, \dots)$. A specific Ω direction and a reference tetrahedron denoted by $\mathcal{T}_r = (\mathbf{P}_1, \mathbf{P}_2, \mathbf{P}_3, \mathbf{P}_4)$ with $\mathbf{P}_1 \leq \mathbf{P}_2 \leq \mathbf{P}_3 \leq \mathbf{P}_4$ are considered. ΔP_j ($j = 1, 2, 3, 4$), ΔP_{12} and ΔP_{123} are the plans orthogonal to the Ω direction and are crossed respectively by \mathbf{P}_j , \mathbf{P}_{12} and \mathbf{G}_1 . It should be noted that the integration points \mathbf{i}_f of panels f ($f = 1, 2, \dots, 6$) are defined only from the coordinates of the vertices of \mathcal{T}_r (Fig. 2). If V_{P_1} , V_{P_2} , V_{P_3} and V_{P_4} are partial volumes of \mathcal{T}_r , then $(\mathbf{i}_1, \mathbf{i}_2, \mathbf{i}_3) \in V_{P_1}$, $(\mathbf{i}_1, \mathbf{i}_4, \mathbf{i}_5) \in V_{P_2}$, $(\mathbf{i}_2, \mathbf{i}_4, \mathbf{i}_6) \in V_{P_3}$ and $(\mathbf{i}_3, \mathbf{i}_5, \mathbf{i}_6) \in V_{P_4}$. In this study, \mathbf{i}_f was projected to a point \mathbf{u}_f ($\mathbf{u}_f \leq \mathbf{i}_f$) on one of the plans ΔP_j ($j = 1, 2, 3, 4$), ΔP_{12} or ΔP_{123} . In this way, $\psi_{u_f}^k$ could be lineary interpolated from the three nodes $(\mathbf{P}_1, \mathbf{P}_2, \mathbf{P}_3)$. Node \mathbf{P}_4 could not be used since it is downstream from all integration points \mathbf{i}_f of \mathcal{T}_r . Thus, $\psi_{u_f}^k$ can be expressed by:

$$\psi_{u_f}^k \cong \sum_{n_b=1}^3 \alpha_{f,n_b}^k \psi_{n_b}^k \quad \text{such that} \quad \sum_{n_b=1}^3 \alpha_{f,n_b}^k = 1 \quad \text{and} \quad 0 \leq \alpha_{f,n_b}^k \leq 1 \quad (n_b = 1, 2, 3). \quad (25)$$

Values for the coefficients α_{f,n_b}^k ($f = 1, 2, \dots, 6$; $n_b = 1, 2, 3$) remained to be defined. This interpolation technique was expected to improve the closure relations and the precision of the results. For the construction of points \mathbf{u}_f , two cases related to \mathbf{u}_t ($t = 1, 2, 3$) and \mathbf{u}_v ($v = 4, 5, 6$) needed to be considered. Since $\mathbf{i}_t \in V_{P_1}$ and $\mathbf{P}_1 \leq \mathbf{i}_t$ ($t = 1, 2, 3$) then \mathbf{i}_t was projected (according to the Ω direction) in a point \mathbf{u}_t in the plane ΔP_1 (Fig. 2). Except in particular cases, the radiance at point \mathbf{u}_t was interpolated as: $\alpha_{t,1}^k = 1$, $\alpha_{t,2}^k = \alpha_{t,3}^k = 0$ ($t = 1, 2, 3$).

[Figure 2 about here.]

\mathbf{i}_v ($v = 4, 5, 6$) was projected (according to the Ω direction) in a point \mathbf{u}_v ($\mathbf{u}_v \leq \mathbf{i}_v$) in one of the three plans ΔP_j ($j = 1, 2, 3$). The choice of projection was conditioned by the belonging of \mathbf{i}_v to partial volume. Indeed, $(\mathbf{i}_4, \mathbf{i}_5) \in V_{P_2}$ and $\mathbf{i}_6 \in V_{P_3}$. Also, $(\mathbf{i}_5, \mathbf{i}_6) \in V_{P_4}$. Nevertheless, $(\mathbf{i}_5, \mathbf{i}_6)$ could not be projected in ΔP_4 , since node \mathbf{P}_4 is always

downstream from all integration points. Except in particular cases, the projections and interpolations presented thereafter are defined by the position of $(\mathbf{i}_4, \mathbf{i}_5)$ relative to node \mathbf{P}_2 and \mathbf{i}_6 relative to nodes \mathbf{P}_3 and \mathbf{P}_2 (since $\mathbf{P}_2 \leq \mathbf{P}_3$).

Cases for $(\mathbf{i}_4, \mathbf{i}_5)$:

(a) $\mathbf{P}_2 \leq (\mathbf{i}_4, \mathbf{i}_5)$. Then, $(\mathbf{u}_4, \mathbf{u}_5) \in \Delta_{P_{12}}$ and $\alpha_{v,1}^k = \alpha_{v,2}^k = \frac{1}{2}$, $\alpha_{v,3}^k = 0$ ($v = 4, 5$).

(b) $(\mathbf{i}_4, \mathbf{i}_5) \leq \mathbf{P}_2$. Then, $(\mathbf{u}_4, \mathbf{u}_5) \in \Delta_{P_1}$ and $\alpha_{v,1}^k = 1$, $\alpha_{v,2}^k = \alpha_{v,3}^k = 0$ ($v = 4, 5$).

(c) $\mathbf{i}_4 \leq \mathbf{P}_2 \leq \mathbf{i}_5$. Then, $\mathbf{u}_4 \in \Delta_{P_1}$ and $\alpha_{4,1}^k = 1$, $\alpha_{4,2}^k = \alpha_{4,3}^k = 0$; $\mathbf{u}_5 \in \Delta_{P_{12}}$ and $\alpha_{5,1}^k = \alpha_{5,2}^k = \frac{1}{2}$, $\alpha_{5,3}^k = 0$.

Note that the case $(\mathbf{i}_5 \leq \mathbf{P}_2 \leq \mathbf{i}_4)$ was not considered since by construction $\mathbf{i}_4 \leq \mathbf{i}_5$.

Cases for \mathbf{i}_6 :

(a) $\mathbf{P}_3 \leq \mathbf{i}_6$. Then, $\mathbf{u}_6 \in \Delta_{P_{123}}$ and $\alpha_{6,1}^k = \alpha_{6,2}^k = \alpha_{6,3}^k = \frac{1}{3}$.

(b) $\mathbf{P}_2 \leq \mathbf{i}_6 \leq \mathbf{P}_3$. Then, $\mathbf{u}_6 \in \Delta_{P_{12}}$ and $\alpha_{6,1}^k = \alpha_{6,2}^k = \frac{1}{2}$, $\alpha_{6,3}^k = 0$.

(c) $\mathbf{i}_6 \leq \mathbf{P}_2$. Then, $\mathbf{u}_6 \in \Delta_{P_1}$ and $\alpha_{6,1}^k = 1$, $\alpha_{6,2}^k = \alpha_{6,3}^k = 0$.

Now, particular cases are introduced. For some of them, we reformulate the radiance at points $\mathbf{u}_1, \mathbf{u}_2$ and \mathbf{u}_4 . If only the two plans Δ_{P_1} and Δ_{P_2} are coplanar then, $\alpha_{1,2}^k = 1$, $\alpha_{1,1}^k = \alpha_{1,3}^k = 0$. If the plans Δ_{P_2} and Δ_{P_3} are coplanar and $\mathbf{P}_3 \leq \mathbf{i}_4$ then, $\alpha_{4,1}^k = \alpha_{4,3}^k = \frac{1}{2}$, $\alpha_{4,2}^k = 0$. Now, if the three plans $\Delta_{P_1}, \Delta_{P_2}$ and Δ_{P_3} are coplanar then $\alpha_{1,2}^k = 1$, $\alpha_{1,1}^k = \alpha_{1,3}^k = 0$, $\alpha_{2,3}^k = 1$, $\alpha_{2,1}^k = \alpha_{2,2}^k = 0$ and $\alpha_{4,3}^k = 1$, $\alpha_{4,1}^k = \alpha_{4,2}^k = 0$.

3.6 Solution procedure

3.6.1 Marching order map

Once the angular discretization was fixed, a "marching order map" giving the optimal order in which the nodal nodes of the spatial unstructured grid should be visited was made for each Ω^k discrete angular direction.

3.6.2 Expression of the radiance at P nodal node and in the Ω^k discrete angular direction

Let $\mathcal{E}_{f,P}^k$ be the set of vertices of a \mathcal{T} tetrahedron located upstream from the \mathbf{i}_f integration point (on surface panel f), such that $\mathbf{i}_f \in \Gamma_P$ and $\mathbf{i}_f \in \mathcal{T}$. Then, from (25), $\psi_{u_f}^k$ can be expressed by:

$$\psi_{u_f}^k \cong \sum_{\{n_b \in \mathcal{E}_{f,P}^k\}} \alpha_{f,n_b}^k \psi_{n_b}^k \quad \text{such that} \quad \sum_{\{n_b \in \mathcal{E}_{f,P}^k\}} \alpha_{f,n_b}^k = 1 \quad \text{and} \quad 0 \leq \alpha_{f,n_b}^k \leq 1 \quad \forall n_b \in \mathcal{E}_{f,P}^k. \quad (26)$$

Let Ψ_P^k be the set of surface panels f such that $\mathcal{E}_{f,P}^k$ is not reduced to \mathbf{P} and let Υ_P^k be the set of surface panels f such that \mathbf{P} belongs to $\mathcal{E}_{f,P}^k$ and $\Delta_f^k > 0$. It should be noted that the condition $\Delta_f^k > 0$ is similar to that used in the well known Step scheme and it is a necessary condition to ensure the stability of the proposed numerical scheme [33]. If $(E_u)_P^k$ is

defined as the set of neighbouring upstream nodes from \mathbf{P} , then we can write:

$$\bigcup_{f=1}^{N_f} \{\mathcal{E}_{f,P}^k\} = (E_u)_P^k \cup \mathbf{P}. \quad (27)$$

Let,

$$\begin{aligned} \tilde{D}_{n_b,P}^k &= \sum_{\{f \in \psi_{n_b,P}^k\}} \alpha_{f,n_b}^k D_f^k \quad ; \quad \overline{D}_P^k = \sum_{\{f \in \Upsilon_P^k\}} \alpha_{f,P}^k D_f^k, \\ \tilde{E}_{n_b,P}^k &= \sum_{\{f \in \psi_{n_b,P}^k\}} \alpha_{f,n_b}^k E_f^k \quad ; \quad \overline{E}_P^k = \sum_{\{f \in \Upsilon_P^k\}} \alpha_{f,P}^k E_f^k, \end{aligned} \quad (28)$$

and

$$\Psi_P^k = \bigcup_{\{n_b \in (E_u)_P^k\}} \psi_{n_b,P}^k. \quad (29)$$

Ψ_P^k is decomposed in sub-sets $\psi_{n_b,P}^k$ to identify panels $f \in \Psi_P^k$ and nodes $n_b \in (E_u)_P^k$ such that $\psi_{u_f}^k$ is expressed with $\psi_{n_b}^k$ by the closure relations seen previously. It should be noted that $\psi_{n_b,P}^k$ can also be defined from $\mathcal{E}_{f,P}^k$ and $(E_u)_P^k$.

Indeed, if $f \in \Psi_P^k$ then $f \in \psi_{n_b,P}^k$ if $n_b \in \mathcal{E}_{f,P}^k$. Also, it should be noted that if $f \in \psi_{n_b,P}^k$ then $\Delta_f^k \leq 0$.

Thus, the first and second terms of the right hand side of (24) can be rewritten as:

$$\sum_{f=1}^{N_f} \psi_{u_f}^k D_f^k = \sum_{\{n_b \in (E_u)_P^k\}} \psi_{n_b}^k \tilde{D}_{n_b,P}^k + \psi_P^k \overline{D}_P^k, \quad (30)$$

$$\sum_{f=1}^{N_f} \left\{ \sum_{k'=1}^N \tilde{p}^{k',k} \psi_{u_f}^{k'} \Delta \Omega^{k'} \right\} E_f^k = \sum_{\{n_b \in (E_u)_P^k\}} \left\{ \sum_{k'=1}^N \tilde{p}^{k',k} \psi_{n_b}^{k'} \Delta \Omega^{k'} \right\} \tilde{E}_{n_b,P}^k + \left\{ \sum_{k'=1}^N \tilde{p}^{k',k} \psi_P^{k'} \Delta \Omega^{k'} \right\} \overline{E}_P^k. \quad (31)$$

Finally, combining (15), (24) and (31), an algebraic equation is obtained relating ψ_P^k to the radiances at neighbouring upstream nodes from node \mathbf{P} :

$$\psi_P^k = \frac{b_P^k + c_P^k}{a_P^k}, \quad (32)$$

with,

$$\begin{aligned} a_P^k &= \mu_{t,P} \Delta \Omega^k V_P + \overline{D}_P^k \quad ; \quad b_P^k = - \sum_{\{n_b \in (E_u)_P^k\}} \psi_{n_b}^k \tilde{D}_{n_b,P}^k, \\ c_P^k &= \left\{ \mu_{s,P} \sum_{k'=1}^N \tilde{p}^{k',k} \psi_P^{k'} \Delta \Omega^{k'} + S_P^k \right\} \Delta \Omega^k V_P - \sum_{f=1}^{N_f} C_f^k \\ &\quad - \sum_{\{n_b \in (E_u)_P^k\}} \left\{ \sum_{k'=1}^N \tilde{p}^{k',k} \psi_{n_b}^{k'} \Delta \Omega^{k'} \right\} \tilde{E}_{n_b,P}^k - \left\{ \sum_{k'=1}^N \tilde{p}^{k',k} \psi_P^{k'} \Delta \Omega^{k'} \right\} \overline{E}_P^k. \end{aligned} \quad (33)$$

It should be noted that in Eq. (32), ψ_P^k is independent of downstream radiances and the method is fully explicit (without taking into account the summation term related to scattering).

3.6.3 Iterative procedure and improvement of the convergence rate

An iterative procedure was applied to solve Eq. (32) (for all $k \in \{1, \dots, N_{dir}\}$) with summation term related to scattering. As our numerical method is designed to take into account a refractive index mismatch at the tissue-air interface, the same iterative procedure was used for solving the RTE with these boundary conditions. In order to improve the convergence rate of the computational method, a convergence criterion dealing with the values of the fluence for the interior spatial grid nodes was introduced. The convergence criterion was related to a relative difference and the prescribed tolerance was similar to that use for the convergence criterion of the outgoing flux at the medium surface. It was observed that the convergence of the computational method to the real solution is faster for the spatial grid nodes in the vicinity of the illuminated surface of the medium. In that case, the number of grid nodes that are used for the computation decreases when the number of iterations increases to reach the convergence.

3.6.4 Optimisation of the memory consumption for structured spatial grids

An important point was taken into account linked to the increase of the memory consumption when the spatial grid size increases. From the spatial grid, some geometrical data, that have to be computed once for all, were extracted for each vertice and tetrahedron in order to lessen the computational time. However, the number of tetrahedrons in structured grids tends to be around six times the number of vertices in the grid. Moreover, several other data needed to be stored for each vertice, leading to a mean memory cost per grid vertice that is around 12,500 bytes when the number of vertices is large. As an illustration, the number of tetrahedrons and the memory cost for some typical grid sizes are given in the first three columns of Table 1.

[Table 1 about here.]

As a large part of the memory consumption was related to the spatial grid, this last was compressed by storing the required data for only one instance of each tetrahedron type present in the grid. Then, each tetrahedron in the grid was associated to its representative instance. So, a parallel multi-threaded algorithm that compress any given grid was developed. No particular assumptions were assumed on the input grid, although best results were to be expected for regular or structured grids as it is more likely that they contain a large number of isomorphic tetrahedrons. The global impact of that optimization is shown in the last three columns of Table 1. A memory gain around 30% for large grids was reached. The gains were computed here according to the overall memory consumption. However, if we focus on the optimized part alone, that is to say the geometric information related to the tetrahedrons, our grid optimization decreased

its memory cost to around 1% for large grids, which is a very efficient. Finally, although our compression algorithm is fully adapted to a multi-core machine, it may take significant times for large grids, as the overall complexity is in $O(n^2)$. Fortunately, this compression can be done off-line and only once for a given grid. Moreover, our algorithm can be quite easily extended to a distributed version, well suited to computing clusters.

3.6.5 Parallel implementation

In our previous study, a first multi-threaded parallel version of the 2D computational method was developed for a single multi-core machine using OpenMP [34]. This version exploited the independent calculations related to the Ω^k discrete angular directions of light propagation. As the initial version was extended to the 3D geometry, the impact of the memory consumption had become a major issue, as previously discussed. Moreover, the 3D calculations are time consuming. Those two reasons had led us to develop a distributed version of the 3D computational method. So, our OpenMP multi-threaded algorithm was extended to a distributed version using also the MPI communication library [35]. As it is essential in distributed computing to minimize the communications between the machines, we have naturally chosen to distribute the computations over the discrete angular directions. Hence, the parallel scheme has two levels of parallelism. The former is the distribution of the angular directions over the machines. The latter is the multi-core parallel processing of the subset of angular directions allocated to each machine. This provided an efficient version of the computational method that takes advantage of computing clusters. The second interest of distributing the algorithm was to decrease the memory costs on each machine. However, it was not possible to distribute everything because many data were required for every discrete angular direction. Typically, the grid had to be duplicated. Fortunately, we saw above that its memory cost was strongly lessen with the compressed grid. On the opposite, some other data can be distributed over the set of machines, such as all data depending on the angular directions, including the radiances computed at each node of the spatial grid. This provided a significant reduction of the memory consumption on each machine, but in counterpart, it required explicit communications between the machines to take into account the radiances for all directions. Those informations were needed on every machine, at the end of each iteration in the convergence procedure. This corresponds to a multiple-broadcast, where each machine had to send its own data to all other machines. Efficient algorithms exist in classical communication libraries like MPI, but the problem is the memory cost. In order to preserve the reduced memory consumption, each machine stored the data coming from only one other machine at a time. So, a circular data exchange was used among the machines, logically organized in a ring topology. Several communication schemes are possible to perform this global exchange. A first solution (S_1) is that the piece of data from each machine crosses the ring from

neighbor to neighbor in a given (arbitrary) direction. The data are exploited by each machine during the ring traversal. The major drawback of that method is that it requires two communication buffers for the simultaneous send/receive operations. Another solution (S_2), that requires only one communication buffer, is that each machine receives external data from a machine at a given distance in the ring and sends its own data to another machine at the same distance but in the other direction along the ring. Those exchanges are performed simultaneously over the entire set of machines. In Figure 3 are depicted the first stages of this communication process, where the arrows represent the data transfers.

[Figure 3 about here.]

The choice between S_1 and S_2 depends on the hardware context and topological organization of the set of machines. In local clusters with homogeneous links between machines, it should not make strong differences. However, if the interconnection network is heterogeneous or contains hierarchical levels, the former solution S_1 should provide better performance whenever the logical neighbors are chosen according to the fastest links. Nevertheless, for very large meshes processed on systems with limited memory, the latter solution S_2 should be privileged as there is an additional memory cost around 5% of the total amount. Finally, we obtain a hierarchical algorithm with a high level of distribution between the machines of the system, as well as a multi-threaded level of parallelism inside each node.

4 Results and discussion

4.1 Configuration of the physical model

A model domain represented by a three-dimensional homogeneous cubic enclosure of size $L_x \times L_y \times L_z$ with $L_x = 1$ mm or 10 mm, $L_y = L_z = 12$ mm was considered. For all the case studies, the refractive index of the outside medium (air) was set to one. The medium surface at $x = 0$ mm was illuminated with a perpendicular incident laser beam. The spatial position $\mathbf{r}_w = (0, \mathbf{r}_{wy}, \mathbf{r}_{wz})$ denotes any point on the illuminated bounding surface of the medium and the radius ρ is defined as $\rho = \sqrt{\mathbf{r}_{wy}^2 + \mathbf{r}_{wz}^2}$. The optical properties of the medium are listed in Table 2. The numerical simulations were carried out using a computational spatial grid composed of ($n_x \times n_y \times n_z = n_{xyz}$) nodes (n_x, n_y, n_z according to the (Ox), (Oy), (Oz)-axis, respectively). For ease of implementation, structured grids, with nodes arranged along straight lines, were employed for all investigations presented here. When it is not specified, the angular domain was subdivided into 256 ($=16 \times 16$) discrete angular directions with 8×8 subdivisions into a solid angle for normalization of the phase function. A preliminary angular grid-refinement study indicated that this angular discretization was sufficient to ensure a good solution accuracy. The iterative procedure continued until the relative difference between the values of the outgoing

flux at the bounding surface of the medium, from one iteration to the next, decreased below a prescribed tolerance. In the selected problems considered here, a tolerance set to 10^{-5} was found to be satisfactory. The obtained solutions are validated against those of the MC method provided by Kienle [38], which is expected to converge in the limit of an infinitely large number of simulated photons to the exact solution of the RTE [36].

4.2 Elastically scattered light

The lateral intensity profile of the collimated incident beam was modeled by a Gaussian function according to:

$$\Upsilon(\rho) = \frac{2}{\pi \sigma^2} \exp\left(-\frac{2\rho^2}{\sigma^2}\right), \quad (34)$$

where σ is the beam width. In order to capture the shape of the incident Gaussian beam, the spatial grid (in the plane (Oyz)) was refined around the strong variation of the Gaussian function. Table 2 gives the parameters used in the simulations where several optical properties of the medium were considered. Table 3 gives the spatial and angular discretizations and the number of iterations needed to obtain a converged solution for each case studied.

[Table 2 about here.]

[Table 3 about here.]

In the first test case (see Tables 2 and 3), the multiple scattering regime has then to be considered since the transport mean free path l_t [37] is equal to 1 mm. To correctly take into account the first scattering events in the medium ($l_s = 0.2$ mm), the first node (according to the (Ox) -axis) from the bounding surface of the medium at $x = 0$ mm was located at 0.1 mm. Fig. 4(a) shows the steady-state spatially resolved reflectance (at $x = 0$ mm) along the centerline $z > 0$ mm obtained with the MFVM based on the Exponential scheme. Obviously, the magnitudes for reflectance decrease with the increase of the radial position ρ . It can be seen that the solution given by the MFVM based on the Exponential scheme is in good agreement with the MC solution used as a reference. Ray effect and False scattering [29] cause mainly the small relative differences which do not exceed here 1.5% (see Fig. 5(a)) with the grid considered. The MC solution gives statistical errors up to 0.4% in that case [38]. In the second test case, the scattering coefficient was higher with $\mu_s = 10 \text{ mm}^{-1}$ (Table 2). Then, a finer spatial grid was applied (Table 3) with more nodes used in the vicinity of the source to correctly take into account the first scattering events in the medium ($l_s = 0.1$ mm). The steady-state spatially resolved reflectance along the centerline $z > 0$ mm is shown in Fig. 4(b). Compared to the first case, the magnitude of the reflectance is higher since more scattering events occurred in the medium. So, more iterations were required for convergence (see Table 3). A good agreement is observed when the MFVM (based on the Exponential scheme) solution is compared to the MC

solution and the relative differences do not exceed here 1% (Fig. 5(a)). In the third test case, the absorption coefficient was higher with $\mu_a = 0.1 \text{ mm}^{-1}$ and the other optical properties were the same as in test case 2 (Table 2). There is more light attenuation in the medium leading to decrease the backscattered light. Compared to test case 2, the magnitude of the reflectance is then lower especially at larger distances (Fig. 4(c)). Hence, more spatial grid nodes (Table 3) mainly in the vicinity of the source were needed to better represent the first absorption events in the medium. The number of iterations is lower (compared to test case 2) due to the light attenuation in the medium. In the fourth test case, the H-G phase function was considered with a different value of the anisotropy factor, set to 0.9. The other optical properties were the same as in second test case (Table 2). Hence, a finer angular discretization was used to well represent the highly forward scattering (see Table 3). An angular grid-refinement has to be accompanied by a spatial grid-refinement, that's why the number of spatial grid nodes is of the same order as in third test case. Figs. 4(d) and 5(a) show that even for a highly forward scattering medium, the MFVM (based on the Exponential scheme) succeeded to obtain a good accuracy. In the fifth test case, the width of the Gaussian beam was reduced to 0.3 mm. Fig. 4(e) shows the change in the curve shape for the reflectance in the vicinity of the laser source and that the MFVM (based on the Exponential scheme) solution is accurate even in that case (Fig. 5(a)). In the last test case, the medium and the outside medium (air) have the same value for the refractive index set to one (see Table 2). So, there is no reflection at the tissue-air interface. Hence, the magnitude of reflectance is higher near the laser source compared to that of case 2. The relative differences between the two solutions (when the MFVM is used with the Exponential scheme) do not exceed here 1.5% (Fig. 5(a)).

[Figure 4 about here.]

The Step scheme, which is equivalent to the first order Upwind scheme, is probably the most widely used in the deterministic numerical methods such as the FDM, FVM or the FEM for solving light propagation in biological tissues. It therefore seemed necessary to implement the Step scheme in the MFVM. Its results are compared with those obtained using the Exponential scheme. Fig. 2 shows the steady-state spatially resolved reflectance along the centerline $z > 0$ mm obtained with the MFVM based on the Step scheme for all the cases presented before. Fig. 5(b) shows the relative differences when the solution is compared with MC reference solution.

The same spatial and angular grids were used for each case as, presented in Table 3. Although the MFVM with the Step scheme is faster (about three times faster than the MFVM based on the Exponential scheme), the results show that it tends to overpredict the reflectance leading to relative differences up to 60% (Fig. 5(b)). Very poor predictions are given for large values of the radius ρ . The increase of errors is due to false scattering which is excessively introduced by the Step scheme. False scattering is associated with the spatial discretization scheme and arises in multidimensional problems

when the light beams are not aligned with the spatial grid lines.

[Figure 5 about here.]

Ray effects and false scattering are two major sources of inaccuracy of the MFVM. However, they may be mitigated by refining the angular and spatial discretizations. Although the origin of the two errors is different, there is an interaction between them, since they tend to compensate each other. It was shown that decreasing one of the errors while keeping the other unchanged may decrease the solution accuracy because the compensation effect disappears. This implies that simultaneous spatial and angular refinement, or a more accurate spatial differencing scheme and angular refinement, should be used to improve solution accuracy. If only one of these two refinements is made, the solution accuracy may decrease. To quantify the inaccuracy due to ray effects and false scattering, the sensitivity of the MFVM (based on the Exponential scheme) to the spatial and angular discretizations for case 4 is presented in Fig. 6. When the angular discretization is prescribed to 24×24 directions, the relative differences increase with coarser spatial grids (red, blue and black solid lines curves). When the spatial discretization is prescribed to 6,543,371 nodes, the relative differences increase with coarser angular discretizations (red curves). When a combination of coarser spatial and angular grids is considered, the relative differences obviously increase more. It can be seen however that the solution accuracy for 1,382,589 nodes and 24×24 directions is not better than for 1,382,589 nodes and 16×16 directions. As expected, there is not in the first case the compensation effect due to ray effects and false scattering. It can be found that for each case studied, the number of iterations required for convergence in the MFVM is moderately lower for the Step scheme than the Exponential scheme (see Table 3).

[Figure 6 about here.]

Fig. 7 is given to show that the solution of the MFVM (based on the exponential scheme) obtained at different iterations predicts light propagation in the medium for the corresponding different scattering orders. The figure shows the spatially resolved reflectance for single, double and triple scattering.

[Figure 7 about here.]

4.3 Fluorescence light

In the model of fluorescence light, two coupled RTEs have to be solved. Thus, to reduce the computational time and the memory space due to the finer spatial grid needed in fluorescence simulations, the results are shown for a medium depth L_x equal to 1 mm. Table 4 gives the parameters of simulations.

[Table 4 about here.]

The lateral intensity profile of the perpendicular incident beam was modeled either with a Gaussian function (Eq. (34)) or a flat function according to:

$$\Upsilon(\rho) = \frac{1}{\pi \sigma^2} \quad \text{if } 0 < \rho \leq 1 \text{ mm} \quad \text{and} \quad \Upsilon(\rho) = 0 \quad \text{otherwise.} \quad (35)$$

The computational domain consisted of 718,725 and 750,141 nodes when the illumination was performed with the Gaussian and flat functions, respectively. The angular discretization (16×16 directions with 8×8 subdivisions into a solid angle for normalization of the phase function) was the same in both cases. It can be seen that the numerical solution given by the MFVM with the Exponential scheme is in good agreement with the MC solution (Fig. 8). In both cases, the relative differences do not exceed 1.5% (Fig. 9). The Step scheme, meanwhile, yields larger differences up to 5% (Fig. 9(b)).

[Figure 8 about here.]

[Figure 9 about here.]

The sensitivity of the MFVM (based on the Exponential scheme) to the spatial and angular discretizations when the illumination was performed with the Gaussian beam is depicted in Fig. 10. Relatively accurate results were obtained on coarse grids and the relative differences were found to decrease with spatial and angular grid refinements. It can be seen that the solution is more sensitive to the angular discretization. Indeed, with the finer spatial grid and the coarser angular discretization, the relative differences reach about 23%. And, the differences increase with coarser spatial grids, whereas with the finer angular discretization and whatever the spatial grid, the relative differences are less than 10%.

[Figure 10 about here.]

4.4 Parallel algorithm

In order to evaluate the quality of the parallel algorithm, this one was tested on test case 1 with the Grid'5000 platform [39], with 8 nodes containing: 2 CPUs Intel Xeon E5-2630 v3, 8 cores/CPU, 126GB RAM, 2×558GB HDD, 10Gbps ethernet. The spatial grid was composed of 805,879 nodes and 4,680,000 tetrahedrons. The number of discrete angular directions was 256 (16×16), which induced that the maximal number of required machines was 16 (16 machines with 16 cores each). In Table 5, the performance results of our parallel computational method are presented.

[Table 5 about here.]

First of all, it can be observed that significant speedups were obtained when increasing the number of machines. However, as expected in presence of global data exchanges, the efficiency decreases due to the additional cost of communications between machines. That cost increases with the number of machines as the global exchanges imply a number of data transfers that is polynomial in function of the number of machines whereas messages sizes decrease linearly when the number of machines increases. In Table 6 are given the percentages of the time spent in performing communications during the process. A significant increase up to around 25% for the maximal number of machines can be observed for both strategies. However, the efficiency loss stays quite limited for the maximal number of needed machines (around 30% for 16 machines). In this context of a local cluster, it is confirmed that there is no great difference between both strategies S_1 and S_2 . Additional experiments have been performed with a larger grid (around 3 millions of nodes) and the global efficiency loss from S_1 to S_2 was never larger than 1%.

[Table 6 about here.]

5 Conclusion

This paper reports a new efficient numerical solution of the 3D RTE. Both elastically scattered light and fluorescence light through a biological tissue illuminated by a collimated incident beam were studied. The proposed deterministic computational method was applied to several test problems and the solutions were compared with MC reference solutions. A good level of accuracy was obtained with the Exponential scheme which reduces efficiently the false scattering. To our knowledge, this is the first time that a deterministic numerical method achieves such a precision for the studied problems. The Exponential scheme is significantly more accurate than the Step scheme, at the expense of additional computational time. It is the best alternative regarding the compromise between accuracy and computational requirements. Concerning the parallel computing, the simulations showed a limited loss of efficiency with the maximal hardware resources corresponding to the degree of parallelism, despite the global data exchanges. Additional levels of parallel computing may be added by using new generation hardware accelerators such as GPUs.

In future research, we plan to use our computational method in optical tomography (as an accurate forward solver in the inverse problem) that reconstruct the optical properties of biological media (containing for example tumor-like inclusions or fluorescent sources) based on reflectance measurements collected at the tissue surface.

References

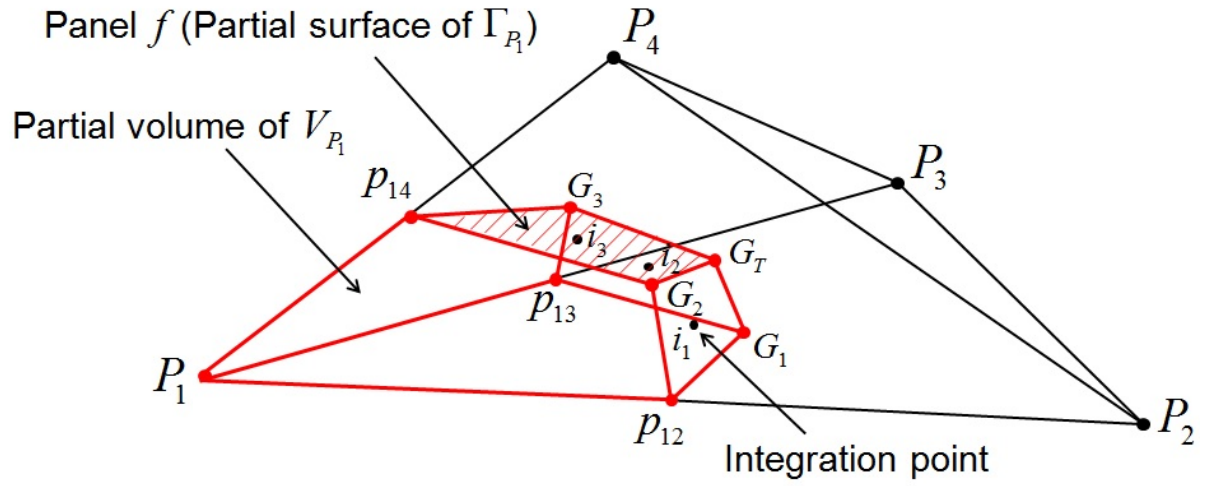
- [1] Arridge SR. Optical Tomography in Medical Imaging, Topical Review. *Inv P* 1999;15:R41-R93.
- [2] Ntziachristos V. Fluorescence molecular imaging. *Annu Rev Biomed Eng* 2006;8:1-33.
- [3] Arridge SR, Schotland JC. Optical Tomography: forward and inverse problems. *Inv P* 2009;25(12):123010.
- [4] Klose AD. Light Scattering. Reviews 4, Book Chapter: Radiative transfer of luminescence light in biological tissue. Berlin Heidelberg: Springer;293-345; 2009.
- [5] Katika KM, Pilon L. Steady-state directional diffuse reflectance and fluorescence of human skin. *Appl Opt* 2006;45(17):4174-4183.
- [6] Yudovsky D, Pilon L. Modeling the local excitation fluence rate and fluorescence emission in absorbing and strongly scattering multilayered media. *Appl Opt* 2010;49(31):6072-6084.
- [7] Katika KM, Pilon L. Feasibility analysis of an epidermal glucose sensor based on time-resolved fluorescence. *Appl Opt* 2007;46(16):3359-3368.
- [8] Klose AD, Hielscher AH. Fluorescence tomography with the equation of radiative transfer for molecular imaging. *Opt Let* 2003;28(12):1019-1021.
- [9] Kim HK, Lee JH, Hielscher AH. PDE-constrained Fluorescence Tomography with the Frequency-Domain Equation of Radiative Transfer. *IEEE Journal of Selected Topics in Quantum Electronics* 2010;16(4):793-803.
- [10] Kim AD, Moscoso M. Radiative transport theory for optical molecular imaging. *Inv P* 2006;22:23-42.
- [11] Quan H, Guo Z. Fast 3-D optical imaging with transient fluorescence signals. *Opt Exp* 2004;12(3):449-457.
- [12] Gorpas D, Andersson-Engel S. Evaluation of a radiative transfer equation and diffusion approximation hybrid forward solver for fluorescence molecular imaging. *J Biomed Opt* 2012;17(12):126010.
- [13] Guo Z, Kumar S. Three-dimensional discrete ordinates method in transient radiative transfer. *J Therm Heat Trans* 2002;16(3):289-296.
- [14] Guo Z, Kim KH. Ultrafast-laser-radiation transfer in heterogeneous tissues with the discrete-ordinates method. *Appl Opt* 2003;42(16):2897-2905.

- [15] Chai JC, Hsub PF, Lama YC. Three-dimensional transient radiative transfer modeling using the finite-volume method. *J Quant Spectrosc Radiat Transfer* 2004;86:299-313.
- [16] Klose AD, Ntziachristos V, Hielscher AH. The inverse source problem based on the radiative transfer equation in optical molecular imaging. *J Comp Phys* 2005;202:323-345.
- [17] Boulanger J, Charette A. Numerical developments for short-pulsed Near Infra-Red laser spectroscopy. Part I: Direct treatment. *J Quant Spectrosc Radiat Transfer* 2005;91(2):189-209.
- [18] Chu M, Vishwanath K, Klose AD, Dehghani H. Light transport in biological tissue using three-dimensional frequency-domain simplified spherical harmonics equations. *Phys Med Biol* 2009;54:2493-2509.
- [19] Akamatsu M, Guo Z. Ultrafast radiative heat transfer in three-dimensional highly-scattering media subjected to pulse train irradiation. *Numer Heat Transf A* 2011;59(9):653-671.
- [20] Akamatsu M, Guo Z. Transient prediction of radiation response in a 3-D scattering-absorbing medium subjected to a collimated short square pulse train. *Numer Heat Transf A* 2013;63:327-346.
- [21] Akamatsu M, Guo Z. Comparison of transmitted pulse trains predicted by Duhamel's superposition theorem and direct pulse simulation in a 3D discrete ordinates system. *Numer Heat Transf B* 2013;63:189-203.
- [22] Ren K, Abdoulaev G, Bal G, Hielscher AH. Algorithm for solving the equation of radiative transfer in the frequency domain. *Opt Lett* 2004;29(6):578-580.
- [23] Montejo LD, Klose AD, Hielscher AH. Implementation of the equation of radiative transfer on block-structured grids for modeling light propagation in tissue. *Biomed Opt Exp* 2010;1(3):861-878.
- [24] Abdoulaev G, Hielscher AH. Three-dimensional optical tomography with the equation of radiative transfer. *J Elect Imag* 2003;12(4):594-60.
- [25] Kim HK, Netz UJ, Beuthan J and Hielscher AH. Optimal source-modulation frequencies for transport theory based optical tomography of small-tissue volumes, *Opt Exp* 2008;16(22):18082-18101.
- [26] Kim HK, Hielscher AH. A PDE-constrained SQP algorithm for optical tomography based on the frequency-domain equation of radiative transfer, *Inv P* 2009;25(1):015010.
- [27] Kim HK, Flexman ML, Yamashiro DJ, Kendel JJ, Hielscher AH. PDE-constrained multispectral imaging of tissue chromophores with the equation of radiative transfer. *Biomed Opt Exp* 2010;1(3):812-824.

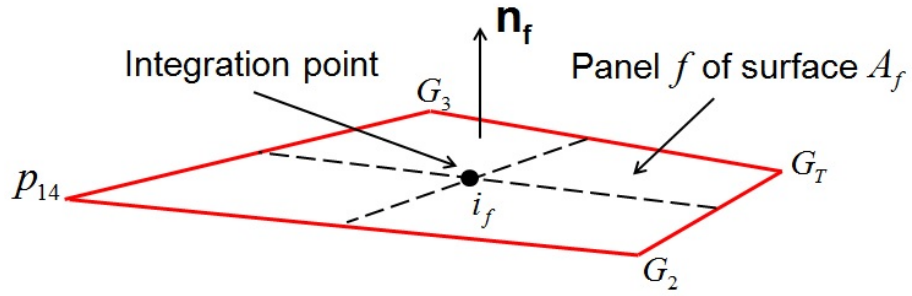
- [28] Mohan PS, Tarvainen T, Schweiger M, Pulkkinen A, Arridge SR. Variable order spherical harmonic expansion scheme for the radiative transport equation using finite elements. *J Comp Phy* 2011;230:7364-7383.
- [29] Modest M. Radiative Heat Transfer. Second ed. San Diego: Academic Press; 2003.
- [30] Long F, Li F, Intes X, Kotha SP. Radiative transfer equation modeling by streamline diffusion modified continuous Galerkin method. *J Biomed Opt* 2016;21(3):36003.
- [31] Coelho PJ. The role of ray effects and false scattering on the accuracy of the standard and modified discrete ordinates methods. *J Quant Spectrosc Radiat Transfer* 2002;73:231-238.
- [32] Hunter B, Guo Z. Numerical smearing, ray effect, and angular false scattering in radiation transfer computation. *IJHMT* 2015;81:63-74.
- [33] Coelho PJ. Advances in the discrete ordinates and finite volume methods for the solution of radiative heat transfer problems in participating media. Review, *J Quant Spectrosc Radiat Transfer* 2014;145:121-146.
- [34] Asllanaj F, Contassot-Vivier S, Liemert A, Kienle A. Radiative transfer equation for predicting light propagation in biological media: comparison of a modified finite volume method, the Monte Carlo technique and an exact analytical solution. *J Biomed Opt* 2014;19(1):015002.
- [35] Vialle S, Contassot-Vivier S. Optimization methodology for Parallel Programming of Homogeneous or Hybrid Clusters. In *Patterns for parallel programming on GPUs*, F. Magoules, Saxe-Coburg Publications, 2013.
- [36] Liemert A, Reitzle D, Kienle A. Analytical solutions of the radiative transport equation for turbid and fluorescent layered media. *Scient Reports* 2017;7:3819.
- [37] Ntziachristos V. Going deeper than microscopy: the optical imaging frontier in biology. *Nature methods* 7(8):603-614, 2010.
- [38] Kienle, A. Lichtausbreitung in biologischem Gewebe, dissertation, University of Ulm, 1995.
- [39] Balouek D, Carpen Amarie A, Charrier G, Desprez F, Jeannot E, Jeanvoine E, and Lèbre A, Margery D, Niclausse N, Nussbaum L, Richard O, Pérez C, Quesnel F, Rohr C, Sarzyniec L, Adding Virtualization Capabilities to the Grid'5000 Testbed. *Cloud Computing and Services Science, Communications in Computer and Information Science*, Springer International Publishing, 2013.

List of Figures

1	Partial volume related to a nodal node	26
2	Projection of integration points \mathbf{i}_t ($t = 1, 2, 3$) in a specific direction and a $(\mathbf{P}_1, \mathbf{P}_2, \mathbf{P}_3, \mathbf{P}_4)$ reference tetrahedron.	27
3	First stages of the S_2 strategy for data exchanges between 8 machines. The S_1 strategy is a repetition of the first stage on the left.	28
4	Steady-state spatially resolved reflectance obtained with the Modified Finite Volume Method (MFVM) and Monte Carlo (MC). The MFVM was used with the Exponential and Step schemes.	29
5	Relatives differences for the steady-state spatially resolved reflectance. The Modified Finite Volume Method (MFVM) was compared with the Monte Carlo reference solution. The results are presented for the different cases.	30
6	Sensitivity to the spatial and angular discretizations of the MFVM (used with the Exponential scheme), for test Case 4.	31
7	Steady-state spatially resolved reflectance at different scattering orders, for test Case 1. The results were obtained with Monte Carlo (MC) and the Modified Finite Volume Method (MFVM) combined with the Exponential scheme.	32
8	Steady-state spatially resolved fluorescence reflectance obtained with the Modified Finite Volume Method (MFVM) and Monte Carlo (MC). The MFVM was used with the Exponential and Step schemes. The illumination was performed with Gaussian and flat beams.	33
9	Relatives differences for the steady-state spatially resolved fluorescence reflectance. The Modified Finite Volume Method (MFVM) used with the Exponential and Step schemes was compared with the Monte Carlo reference solution. The illumination was performed with Gaussian and flat beams.	34
10	Sensitivity to the spatial and angular discretizations of the MFVM (used with the Exponential scheme). The illumination was performed with a Gaussian beam.	35



(a) V_{P_1} partial control volume related to P_1 nodal node.



(b) Panel f

Figure 1: Partial volume related to a nodal node

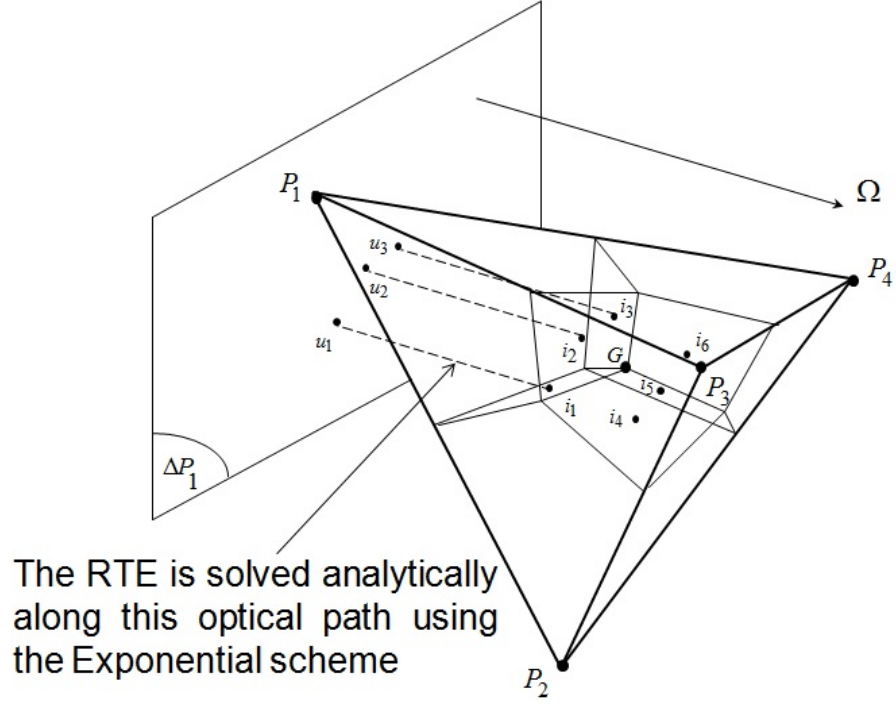


Figure 2: Projection of integration points i_t ($t = 1, 2, 3$) in a specific direction and a (P_1, P_2, P_3, P_4) reference tetrahedron.

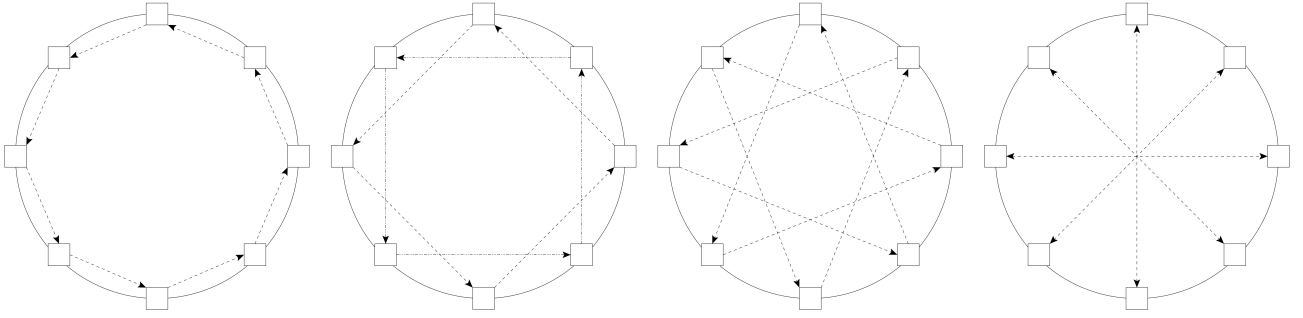
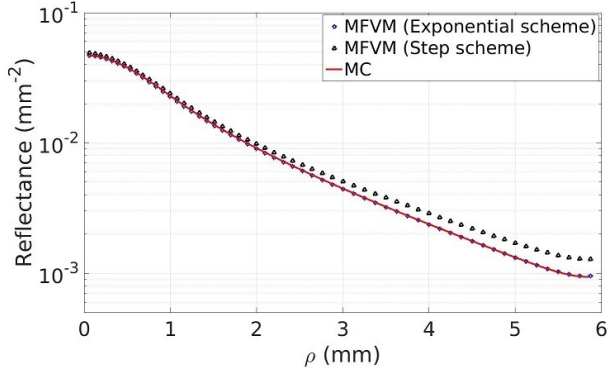
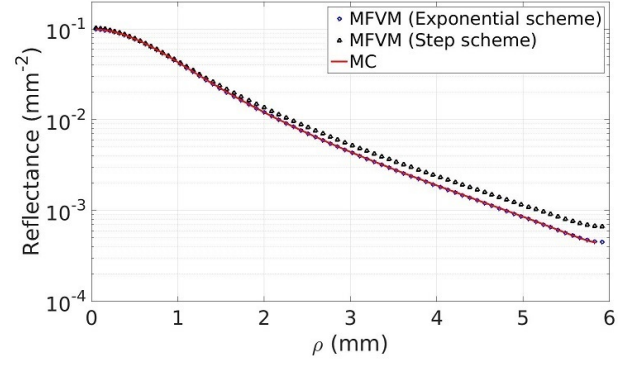


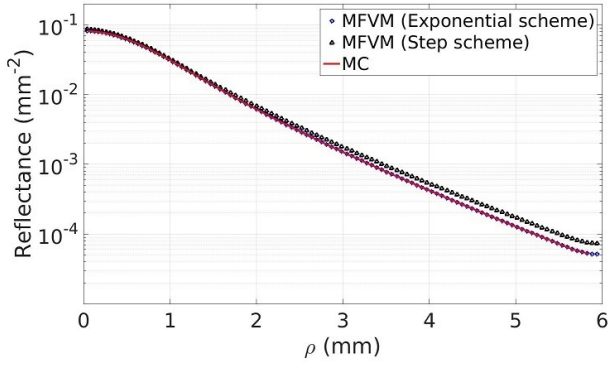
Figure 3: First stages of the S_2 strategy for data exchanges between 8 machines. The S_1 strategy is a repetition of the first stage on the left.



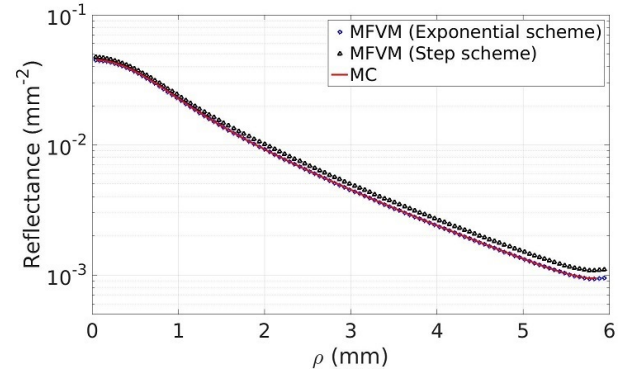
(a) Case 1.



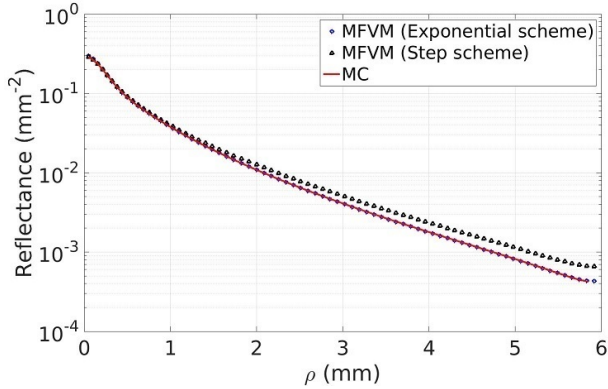
(b) Case 2.



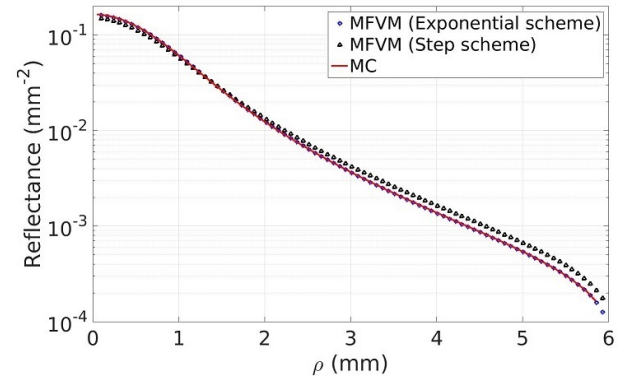
(c) Case 3.



(d) Case 4.

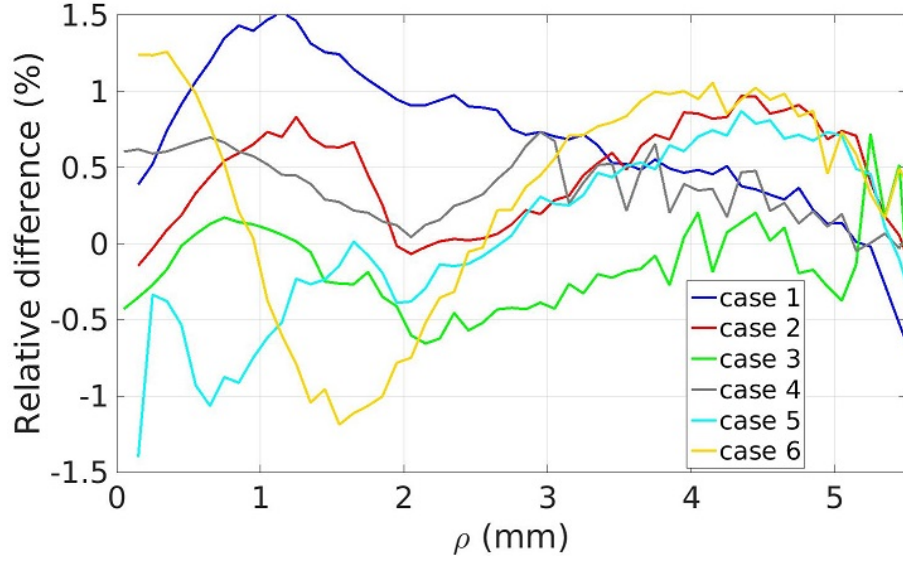


(e) Case 5.

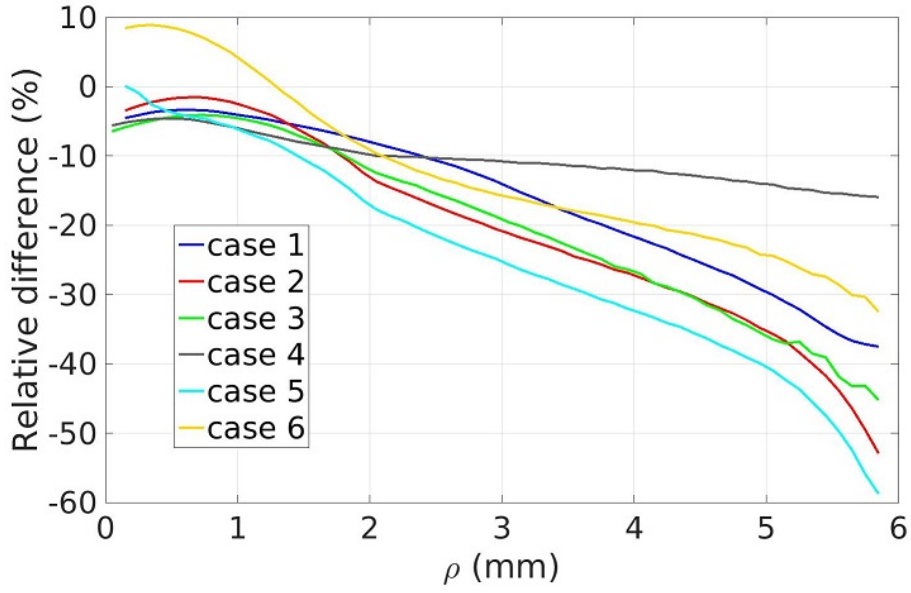


(f) Case 6.

Figure 4: Steady-state spatially resolved reflectance obtained with the Modified Finite Volume Method (MFVM) and Monte Carlo (MC). The MFVM was used with the Exponential and Step schemes.



(a) MFVM used with the Exponential scheme.



(b) MFVM used with the Step scheme.

Figure 5: Relative differences for the steady-state spatially resolved reflectance. The Modified Finite Volume Method (MFVM) was compared with the Monte Carlo reference solution. The results are presented for the different cases.

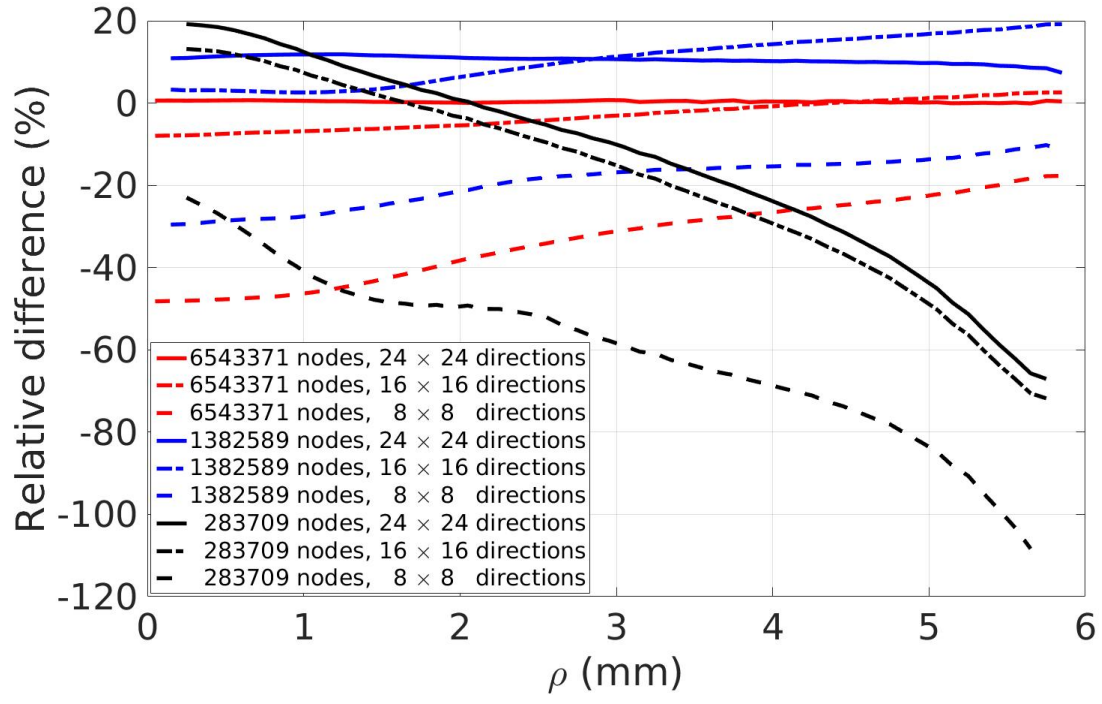


Figure 6: Sensitivity to the spatial and angular discretizations of the MFVM (used with the Exponential scheme), for test Case 4.

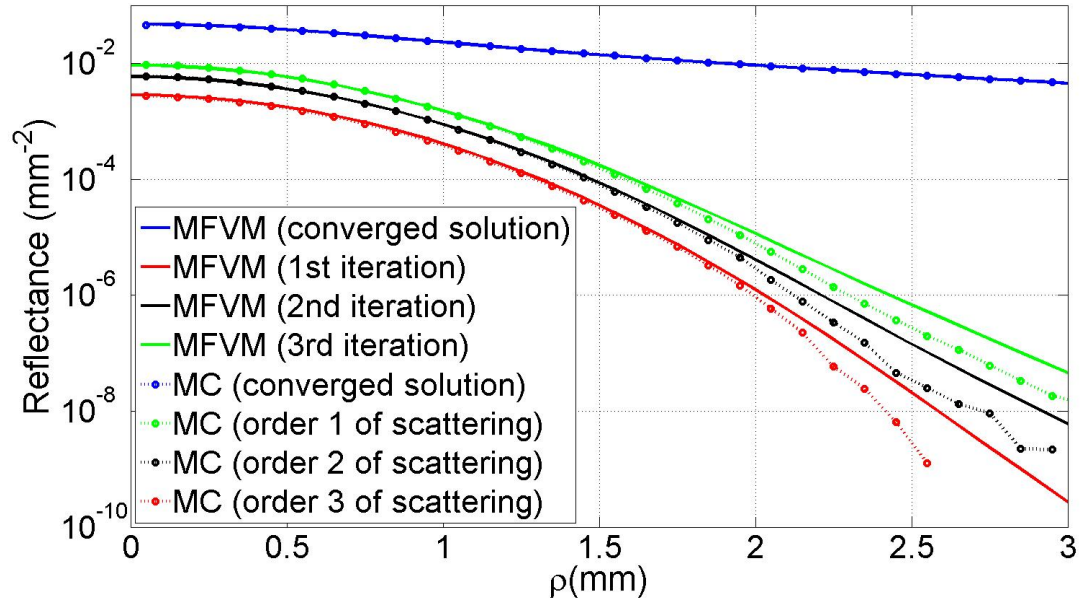
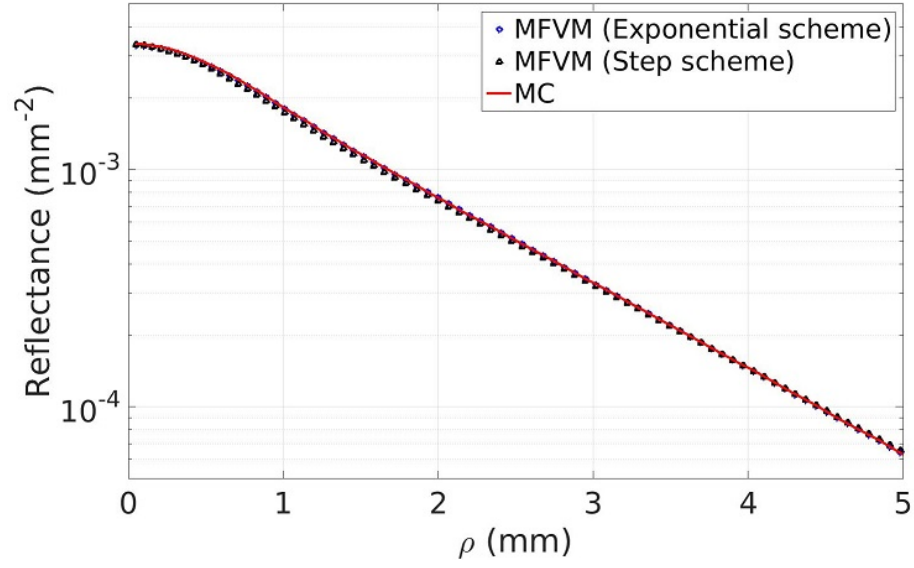
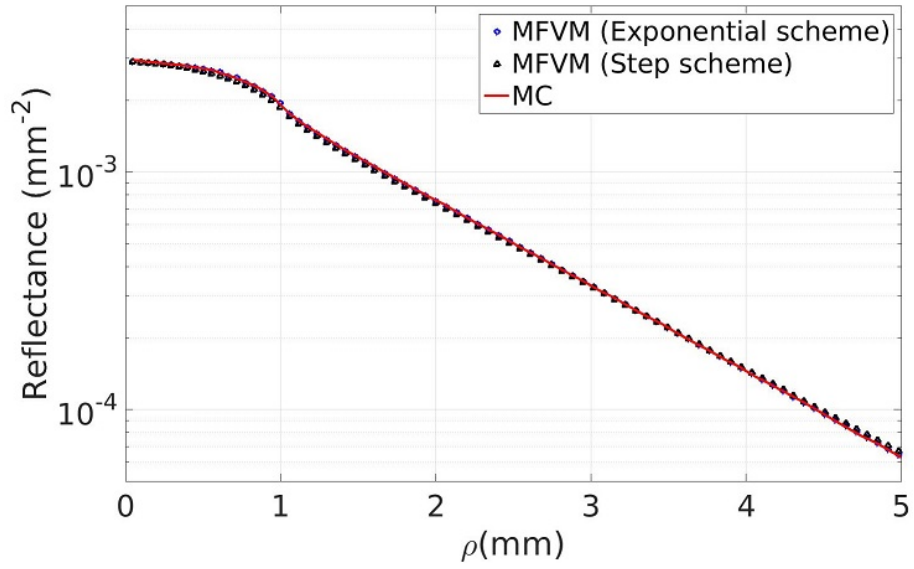


Figure 7: Steady-state spatially resolved reflectance at different scattering orders, for test Case 1. The results were obtained with Monte Carlo (MC) and the Modified Finite Volume Method (MFVM) combined with the Exponential scheme.

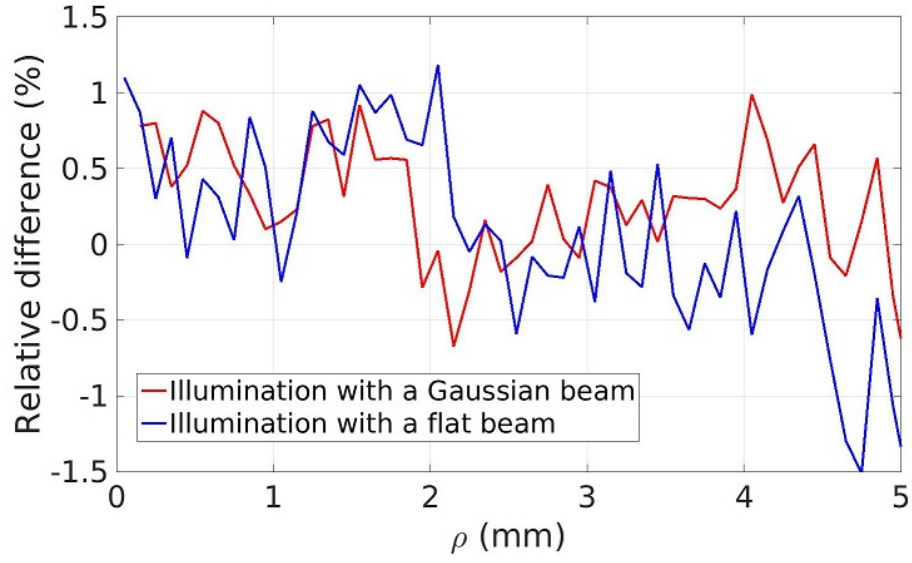


(a) Illumination with a Gaussian beam.

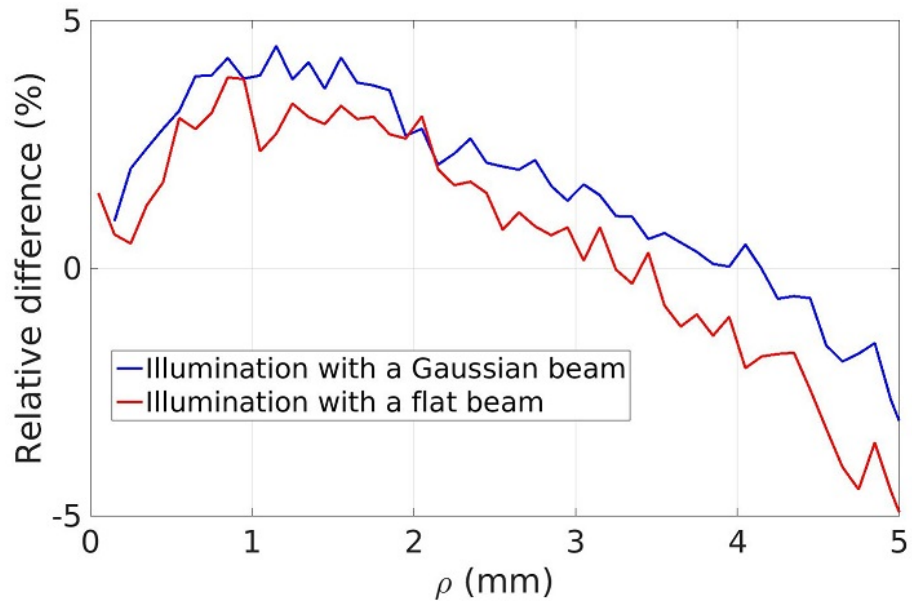


(b) Illumination with a flat beam.

Figure 8: Steady-state spatially resolved fluorescence reflectance obtained with the Modified Finite Volume Method (MFVM) and Monte Carlo (MC). The MFVM was used with the Exponential and Step schemes. The illumination was performed with Gaussian and flat beams.



(a) MFVM used with the Exponential scheme.



(b) MFVM used with the Step scheme.

Figure 9: Relative differences for the steady-state spatially resolved fluorescence reflectance. The Modified Finite Volume Method (MFVM) used with the Exponential and Step schemes was compared with the Monte Carlo reference solution. The illumination was performed with Gaussian and flat beams.

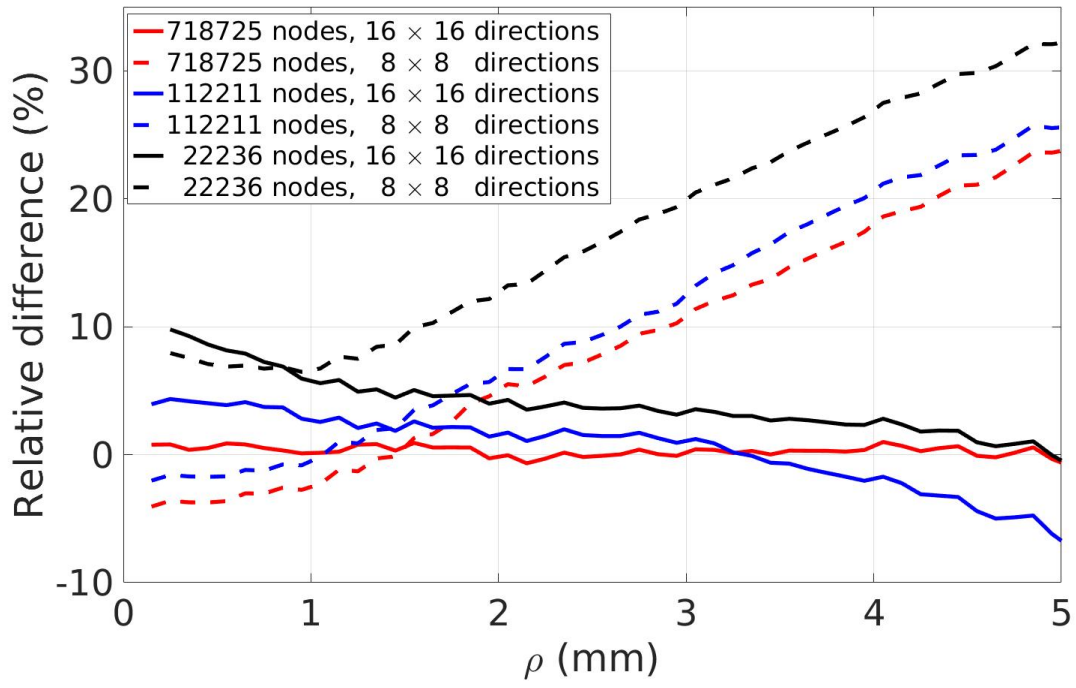


Figure 10: Sensitivity to the spatial and angular discretizations of the MFVM (used with the Exponential scheme). The illumination was performed with a Gaussian beam.

List of Tables

1	Number of tetrahedrons and memory costs for typical spatial grid sizes.	37
2	Parameters used in the simulations for elastically scattered light.	38
3	Spatial and angular grids and number of iterations required for convergence.	39
4	Parameters used in the simulations for fluorescence light.	40
5	Performance of the two communication strategies in function of the number of machines.	41
6	Percentages of communications during the process for both strategies in function of the number of machines.	42

Number of nodes	Normal grid		Compressed grid		Gain (%)
	Number of tetrahedrons	Memory (10^9 bytes)	Number of tetrahedrons	Memory (10^9 bytes)	
1,241	6,144	0.015	2903	0.013	12.99
13,125	69,120	0.161	384	0.118	26.60
112,211	60,0000	1.376	5766	1.005	26.95
805,879	4,680,000	9.674	115320	6.826	29.43
6,584,961	38,880,000	78.688	32448	54.448	30.81

Table 1: Number of tetrahedrons and memory costs for typical spatial grid sizes.

Case	n	g	μ_a (mm ⁻¹)	μ_s (mm ⁻¹)	σ (mm)
1	1.4	0.8	0.01	5	1
2	1.4	0.8	0.01	10	1
3	1.4	0.8	0.1	10	1
4	1.4	0.9	0.01	10	1
5	1.4	0.8	0.01	10	0.3
6	1.0	0.8	0.01	10	1

Table 2: Parameters used in the simulations for elastically scattered light.

Case	Number of spatial grid nodes	Number of angular directions	Number of iterations
1	1,382,589	256 (16×16)	643 (Exponential) / 578 (Step)
2	3,207,033	256 (16×16)	1505 (Exponential) / 1326 (Step)
3	6,451,193	256 (16×16)	879 (Exponential) / 733 (Step)
4	6,543,371	576 (24×24)	1153 (Exponential) / 1037 (Step)
5	3,207,033	256 (16×16)	1503 (Exponential) / 1324 (Step)
6	3,855,735	256 (16×16)	1335 (Exponential) / 1179 (Step)

Table 3: Spatial and angular grids and number of iterations required for convergence.

n	g^x	g^m	$\mu_a^x (\text{mm}^{-1})$	$\mu_a^m (\text{mm}^{-1})$	$\mu_s^x (\text{mm}^{-1})$	$\mu_s^m (\text{mm}^{-1})$	$\mu_a^{x \rightarrow m} (\text{mm}^{-1})$	$\sigma (\text{mm})$	η
1.4	0.8	0.8	0	0.01	7.5	5	0.02	1	1

Table 4: Parameters used in the simulations for fluorescence light.

Number of machines	S_1 communication strategy			S_2 communication strategy		
	Time (s)	Speed-up	Efficiency (%)	Time (s)	Speed-up	Efficiency (%)
1	3782.18	1.00	100.00	3782.18	1.00	100.00
2	1989.88	1.90	95.04	1984.38	1.91	95.30
4	1039.16	3.64	90.99	1054.66	3.59	89.65
8	570.51	6.62	82.87	583.35	6.48	81.04
16	333.24	11.35	70.93	340.23	11.12	69.48

Table 5: Performance of the two communication strategies in function of the number of machines.

Number of machines	2	4	8	16
S_1	4.24	6.87	13.20	25.09
S_2	5.33	8.93	15.88	25.95

Table 6: Percentages of communications during the process for both strategies in function of the number of machines.